Article

High-Performance Composite Separator with a Porous Bicontinuous Structure for Alkaline Water Electrolysis

Liping Liu,* Ju Wang, Guanjun Yang, Shuyuan Wang, Jinyi Wang,* Zhibo Ren, Weiqi Guo, and Peng Liu

Cite This: *ACS Omega* 2025, 10, 9007−9017

Read Online

ACCESS | Metrics & More | Article Recommendations | Supporting Information

ABSTRACT: Alkaline water electrolysis is considered an optimal technology for large-scale production of green hydrogen because of its economic and mature characteristics. The separator plays a crucial role in the alkaline water electrolysis process, as it fulfills the functions of gas separation and electrolyte transport. Nevertheless, the development of advanced separators with low ohmic resistance, high gas barrier ability, and good durability simultaneously remains a major challenge. Here, we first fabricated a series of high-performance composite separators with a porous bicontinuous structure by employing a nonsolvent-induced phase separation technique using a "weak solvent" (a solvent with a low affinity toward the membrane-forming polymer). The unique porous bicontinuous structure endows the membranes with high porosity, narrow pore size distribution with nanopores, and good hydrophilicity. As a result, the composite separator exhibits not only a low area resistance (0.13 Ω·cm^2) but also a high bubble point pressure (5.1 bar). The composite separator also displays excellent durability in both long-term electrolysis and alkaline-aging tests.
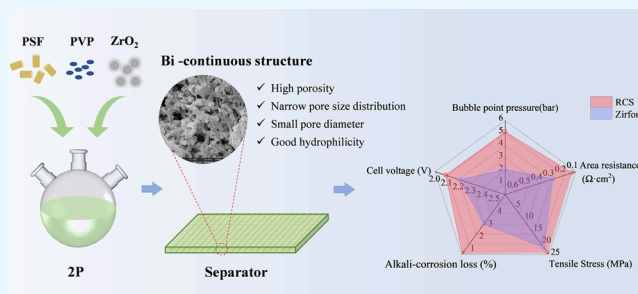
1. INTRODUCTION

The rapid development of renewable energy sources motivated by the increasing serious energy crisis and environmental problems has resulted in new challenges in large-scale energy storage due to the intermittent nature of such sources.[1,2] Hydrogen generation through water electrolysis, a promising green solution for addressing the energy storage issue, has attracted significant attentions due to its advantages of high efficiency, low carbon emission, and high flexibility.[3−6] Among various water electrolysis techniques, alkaline water electrolysis (AWE) is recognized as an optimal choice for coupling with large-scale renewable energy sources due to its low cost (free of noble metal catalysts), simplicity, and high maturity.[7−13] Nevertheless, conventional alkaline water electrolyzers displayed relatively low current densities (0.2−0.4 A cm^{-2}) and slow response time toward dynamic operations (seconds) due to the high ohmic loss through the separator and the low reaction kinetics of the non-noble metal catalysts.[14−17] Additionally, the low partial load toleration of alkaline water electrolyzers is another major concern, and is mainly limited by the gas permeability of the separator.[18−20] Therefore, significant efforts have been made to develop high-performance porous membranes for advanced AWE.

Asbestos was used as the initial porous separator in AWE. It eventually lost its competitiveness because of its carcinogenicity and high-temperature instability.[21,22] Subsequently, polyphenylene sulfide (PPS) fabric separators were used to substitute asbestos in industrial alkaline electrolyzers.[23,24] However, PPS fabric separators generally show a low bubble point pressure (BPP, 0.02 bar) and high ohmic resistance due to their large through-pore diameter and hydrophobic nature, which hinder their further application in advanced alkaline electrolyzers. As an alternative, a new generation of Zirfon-type composite separators consisting of a polymer matrix and hydrophilic nanofillers has been developed with improved performance and great potential for AWE.[25,26] Vermeriren et al.[27] first reported the use of a Zirfon-type composite separator consisting of 80 wt % ZrO$_2$ and 20 wt % polysulfone (PSF) for AWE. The membrane exhibited an area resistance of 0.3 Ω·cm^2 in a 30 wt % KOH electrolyte solution at 20 °C, and the electrolysis system equipped with the membrane displayed a cell voltage of 1.7−1.8 V at 10 kA/m^2 and 120 °C. Kim et al.[28] recently developed an advanced composite separator by constructing a selective skin layer on the surface of a commercial Zirfon separator via ultrasonic spraying method. The membrane showed a narrower pore size distribution and a significantly reduced large-pore fraction compared with the
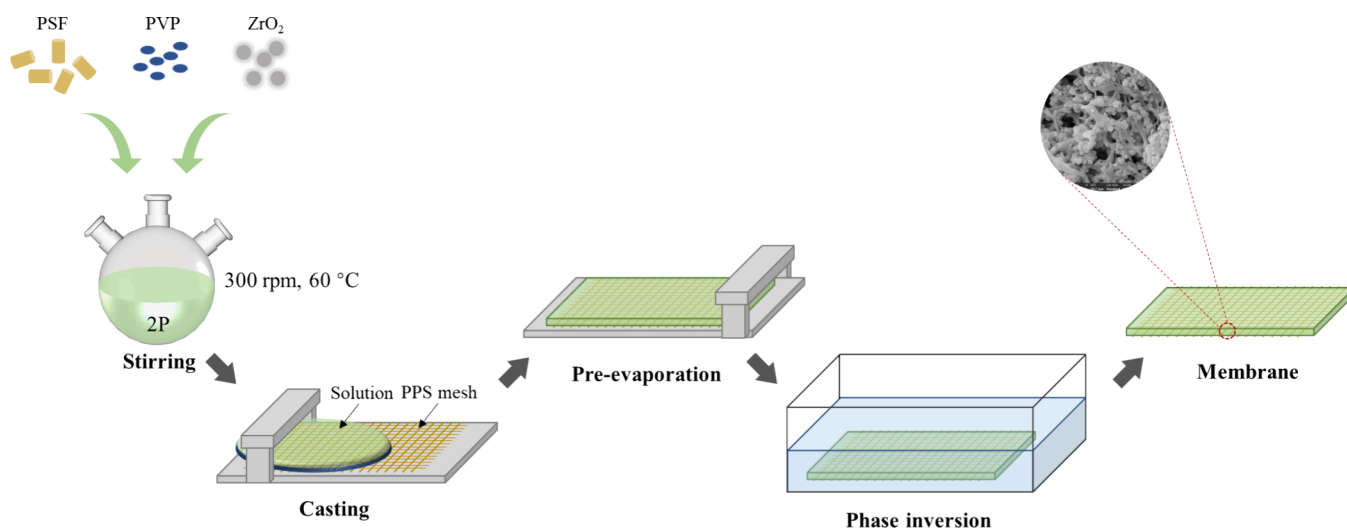
Figure 1. Scheme of the composite separator preparation.

Zirfon membrane. Consequently, the BPP was successfully enhanced to 2.71 bar whereas the area resistance slightly increased to 0.27 $\Omega\cdot cm^2$. Recently, Liao et al.[29] fabricated a thin (268 μm) and flexible composite separator composed of PSF, ZrO_2 nanoparticles, and polypropylene (PP) nonwoven fabric by using a nonsolvent induced phase separation (NIPS) strategy. The composite separator showed an ultrahigh BPP of 24 bar and a low area resistance of 0.14 $\Omega\cdot cm^2$, which were superior to those of the commercial Zirfon. However, the former displayed a substantially lower tensile strength (3.7 MPa). Although significant progress has been made in the development of advanced composite separators,[5,28−32] few composite separators can simultaneously achieve a low ohmic resistance and high gas barrier ability without sacrificing stability. The area resistance of a separator is largely dependent on its wettability and pore structure, whereas the gas barrier ability depends only on the pore structure. Various strategies have been attempted to improve the hydrophilicity of composite separators, including modifying hydrophilic nanofillers, increasing the content of nanofillers, and optimizing the size of the nanofillers.[33−40] In general, the amount of nanofillers in the membranes was adjusted to 85 wt % to maximize the wettability. In the case of pore structure optimization, which is largely dependent on the casting solution system (e.g., cast solution composition and the nature of the solvent and additives) and manufacturing parameters (e.g., pre-evaporation and extraction conditions),[31,32,41−44] the main challenge is achieving a balance between the ionic conductivity and gas barrier ability since a trade-off relationship exists between them. For instance, high porosity facilitates electrolyte transport but is commonly accompanied by macrovoids, which increase the risk of gas permeability, and thus simultaneously achieving a low area resistance and high gas barrier ability becomes difficult. Therefore, designing a porous structure to circumvent this trade-off is crucial for obtaining membranes with excellent overall performance. Bicontinuous-structure membranes are characterized by interconnected open pores and free of macrovoid,[45−47] and can be prepared by employing the conventional NIPS method using a solvent (e.g., 2-pyrrolidone (2P)) with low affinity toward the membrane-forming polymer of PSF.[47,48] These membranes can achieve a good balance between high porosity and narrow pore size.[48,49] It is conceivable that such a porous

structure with an appropriate pore size will provide access to membranes with both low ohmic resistance and high gas barrier ability. To the best of our knowledge, research on the preparation of composite separators with bicontinuous structures and the application of such separators in AWE is scarce.

In this study, we first fabricated a series of bicontinuous-structure composite separators by employing the conventional NIPS method using a 2P solvent with low affinity toward PSF. ZrO_2 nanoparticles were applied as hydrophilic nanofillers due to their advantages of low cost, commercial availability, earth abundance, and chemical stability.[32,50] Different pre-evaporation times were used to regulate the pore sizes of the composite separators. A reinforced composite separator (RCS) was constructed by using PPS mesh as the support layer. Thanks to the unique porous bicontinuous structure, the optimized composite separator exhibits outstanding performance with a high BPP, a low area resistance, and good long-term durability. These findings are expected to provide inspiration for designing high-performance separators for AWE applications.

2. EXPERIMENTAL SECTION

2.1. Preparation of Composite Separators. The preparation process for the composite separators is illustrated in Figure 1. Composite separators were prepared by using the NIPS method. To prepare the casting solutions, PSF (Macklin, China) was dissolved in the 2P solvent (Sigma-Aldrich, USA) via mechanical stirring (300 rpm) at 60 °C for 24 h, and then polyvinylpyrrolidone (PVP, Aladdin, China) and ZrO_2 (Macklin, China, 100 nm) were added. The mass ratio of ZrO_2 to PSF was fixed at 85 wt %/15 wt % due to the trade-off between hydrophilicity and viscosity. All the casting solutions were stored at ambient temperature to degas for more than 24 h. Subsequently, the resultant suspension with a viscosity of 124,931 cP at 25 °C was cast on a glass plate by using a stainless-steel scraper. After the wet membrane was pre-evaporated for a certain time, the resultant membrane was soaked in deionized water for solvent extraction. Previous studies have shown that the pre-evaporation time has a significant effect on the pore structure of membranes and that the growth of the pore structure gradually slows down with the

extension of the pre-evaporation time.[48] Therefore, the pre-evaporation times of 15 s, 1, 2, and 4 min were selected to adjust the pore size for performance optimization. Different composite separators were prepared as per the pre-evaporation times and denoted as CS0.25, CS1, CS2, and CS4, respectively. To prepare the RCS separator, the glass plate was preglued with a PPS mesh material (270 μm, Clever, Japan). The nominal thickness of the composite separators was fixed at 450 μm. Additionally, a commercial Zirfon membrane (PERL UTP 500, Agfa, Belgium) was introduced and labeled as Zirfon. To verify the role of 2P in the preparation process, a membrane denoted as CS-NMP was prepared by using N-methylpyrrolidone (NMP) as the solvent in the casting solution with similar viscosity and the same manufacturing parameters as those used to prepare CS2.

2.2. Characterization. The morphologies of the separators were studied by scanning electron microscopy (SEM, Regulus 8100, Hitachi, Japan). To improve the conductivity of the separators, the samples were sputtered with gold before SEM observation. For cross-sectional morphology analysis, the samples were mechanically fractured in liquid nitrogen.

The BPPs of the separators were measured by using a membrane pore size analyzer (BSD-TD, Beishide, China) according to the GB/T 32361-2015, and the sample size was 3 cm × 3 cm. Prior to the test, the samples were immersed in ethanol to achieve full wetting. The gas pressure corresponding to the first continuous air bubble penetrating the membrane sample was recorded as the BPP. The available maximal gas pressure of the instrument was 35 bar, and its pressure sensitivity was 0.05 mbar. Additionally, the pore size distribution width was estimated from the pore diameters measured by the membrane pore size analyzer using the following equation.

$$W = D_{max} - D_{min} \tag{1}$$

Where W is the pore size distribution width, D_{max} (nm) and D_{min} (nm) are the maximum and minimum pore diameters, respectively.

The porosities of the separators were determined by using a weighing method. The sample size was fixed at 3 cm × 3 cm using a knife mold. Each sample was soaked in deionized water overnight, and the resultant wet separator was weighed after carefully wiping the water droplets from the separator surface with tissue paper. The dry separator was obtained after drying at 50 °C for 2 h in an oven and the mass of the dry separator was measured. The porosity was calculated as follows.

$$\varepsilon = \frac{M_w - M_d}{\rho \times S \times L} \times 100\% \tag{2}$$

where ε is the porosity, M_w (g) and M_d (g) are the masses of the separator in the wet and dry states, respectively, ρ represents the density of deionized water (g·cm^{-3}), S represents the area of the separator sample (cm^2), and L is the separator thickness (cm).

The alkaline absorption ratio (A) was determined as the ratio of the mass of the alkaline-uptake separator to the dry separator counterpart. A sample size of 3 cm × 3 cm was used. The dry separator mass (M_d) was determined after immersing the separator in a deionized water bath overnight and then drying at 50 °C for 4 h. The alkaline-uptake separator mass (M_a) was measured after soaking the separator in a 30 wt % KOH solution for 4 h. The alkaline absorption ratio was calculated as follows.

$$A = \frac{M_a - M_d}{M_d} \times 100\% \tag{3}$$

The wettabilities of the separators were determined by using a contact angle meter (DSA30, Kruss, Germany). Deionized water was used as the infiltrate, and the injection volume of the droplets was 5 μL. A sample size of 5 cm × 1 cm was employed. Prior to the measurements, the separators were dried in an oven at 50 °C for 2 h.

To measure the area resistances of the separators, electrochemical impedance spectroscopy (EIS) was conducted on an electrochemical workstation (IM6, Zahner, Germany) equipped with an H-type cell. The active area of the separator samples was 4.15 cm^2, and a 30 wt % KOH solution was used as the electrolyte for the experiments. EIS measurements were performed under open circuit voltage with an amplitude of 10 mV to minimize the electrode polarization, and the frequency ranged from 100 kHz to 0.1 Hz.

Powder X-ray diffraction (XRD) patterns of the separators were collected on an X-ray diffractometer (Rigaku Ultima IV, Japan) using Cu Kα radiation.

The bulk ZrO$_2$ content of the separator was determined by using inductively coupled plasma optical emission spectrometry (ICP-OES, PE Avio 200, USA).

The tensile strengths of the separators were conducted on an electronic tensile testing instrument (WDW, Xinte, China), and the measurements were performed according to the GB1040.3−2006 standard. The sample size was fixed at 8 cm × 1 cm using a knife mold. The samples were dried in an oven at 50 °C for 2 h before the measurements.

Thermogravimetric (TG) and differential scanning calorimetry (DSC) measurements of the separators were performed (Mettler Toledo, USA) by ramping the temperature from 30 to 800 °C at a rate of 10 °C/min in the air (50 mL/min).

Fourier transform infrared spectroscopy (FTIR) of the separators was performed on a Nicolet iS50 infrared spectrometer (Thermo Fisher Scientific, USA) in air at ambient temperature, and the spectra were collected over the wavenumber range of 600−4000 cm^{-1}.

The corrosion resistance of the separators was assessed by the alkaline-corrosion loss measurements according to the SJ/T 10171.6-91 electronic industry standard. The samples were treated in a 30% KOH solution at 80 °C for 1000 h and weighed before and after the KOH treatment. The alkaline-corrosion loss was calculated by applying the following equation.

$$E = \frac{M_1 - M_2}{M_1} \times 100\% \tag{4}$$

where E is the alkaline-corrosion loss, and M_1 (g) and M_2 (g) are the masses of the dried separator before and after KOH treatment, respectively. The sample size was fixed at 3 cm × 3 cm. Furthermore, the aforementioned experimental data were obtained through three independent tests.

2.3. Electrolysis Tests. Electrolysis experiments of the separators were carried out on a small alkaline water electrolyzer with a zero-gap structure using nickel foams as the cathode and anode. The polarization curve test was performed at 80 °C using an electrolyte solution of 30 wt % KOH. The long-term electrolysis test for 150 h was conducted at 80 °C with a current density of 600 mA cm^{-2} and an electrolyte solution of 30 wt % KOH. The active area of the alkaline water electrolyzer was 25 cm^2.
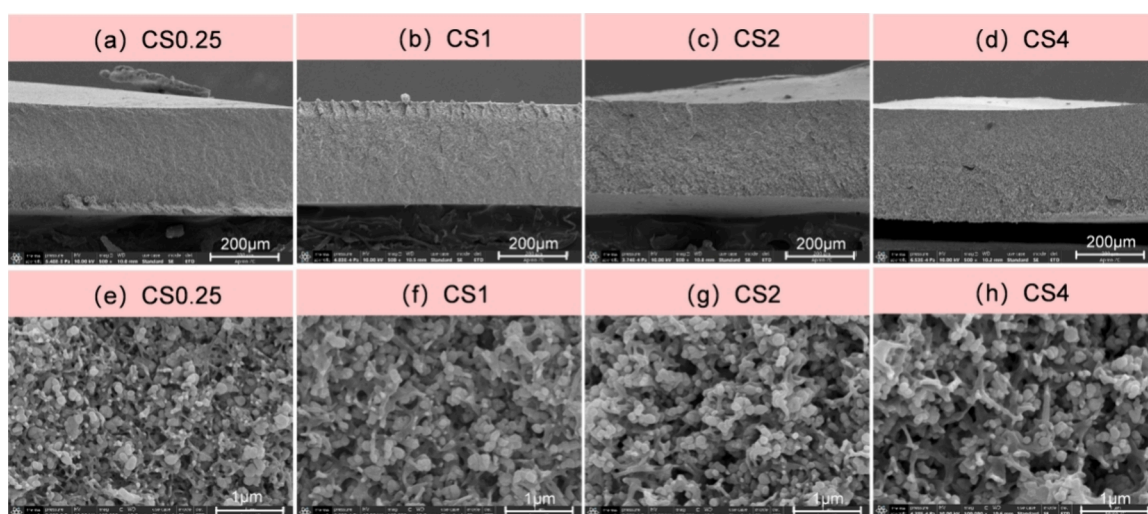
Figure 2. Cross-sectional SEM images of the prepared composite separators: (a−d) At 500× magnification; (e−h) at 100,000× magnification.
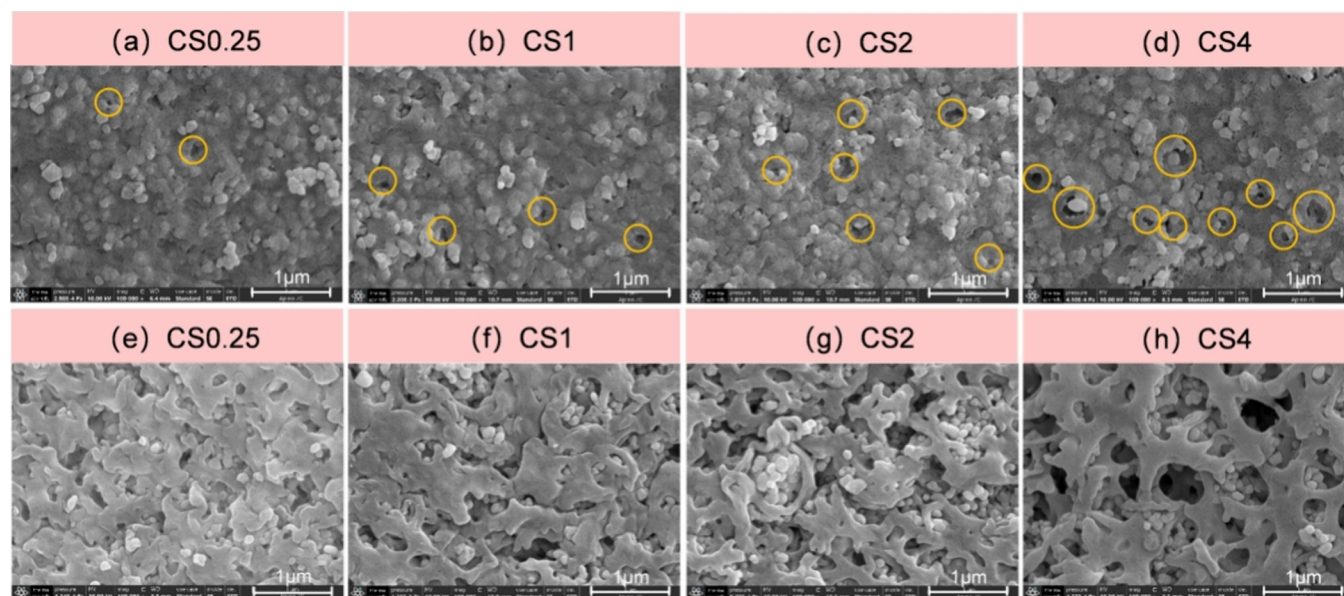

Figure 3. Surface SEM images of the prepared composite separators at 100,000× magnification: (a−d) Top surface; (e−h) bottom surface. The defects on the top surface are marked with yellow circles.

3. RESULTS AND DISCUSSION

3.1. Characterization of the Pristine Composite Separators. *3.1.1. Morphological Structure.* The morphologies of the prepared membranes were characterized by SEM (Figure 2) presents the cross-sectional images of the prepared membranes. For all the prepared membranes, no large macrovoids (e.g., finger-like macrovoids) can be observed in the cross-section. Instead, a porous bicontinuous structure with interconnected pore features forms over the entire cross-section.[48,49] The ZrO$_2$ nanoparticles are uniformly distributed in the membrane and exhibit perfect compatibility with PSF. The pore size increases with the prolonging of pre-evaporation time. Since the ZrO$_2$ nanoparticles are not directly involved in the phase separation process, it is reasonable to assume that they play a negligible role in the phase separation process. To ascertain the impact of 2P on the formation of the porous bicontinuous structure, the CS-NMP membrane was prepared by using NMP as the solvent in the casting solution with similar viscosity. The CS-NMP membrane displays a finger-like

macroporous structure in the cross-section (Figure S1), which confirms that 2P solvent plays an indispensable role in the formation of the porous bicontinuous structure, consistent with the results obtained by Maggay et al.,[49] who found that the affinity of the solvent toward the polymer plays a pertinent role in the morphology of the membranes. It is well-known that the affinity of the solvent toward the polymer can be estimated by using Hansen's solubility parameters of the dispersive forces (δ_D), polar forces (δ_P), and H-bonding (δ_H). The smaller the difference between the solubility parameters of the solvent and the polymer, the better their affinity. As shown in Table S1, the differences between NMP and PSF in δ_D, δ_P and δ_H are very small, confirming that NMP has a high affinity toward PSF. In contrast, the difference between 2P and PSF in δ_D is moderate, but the differences in δ_P and δ_H are significant, demonstrating that 2P has a low affinity toward PSF. Consequently, unlike the introduction of NMP (high affinity toward PSF), the introduction of 2P (low affinity toward PSF) solvent significantly increased the viscosity of the casting
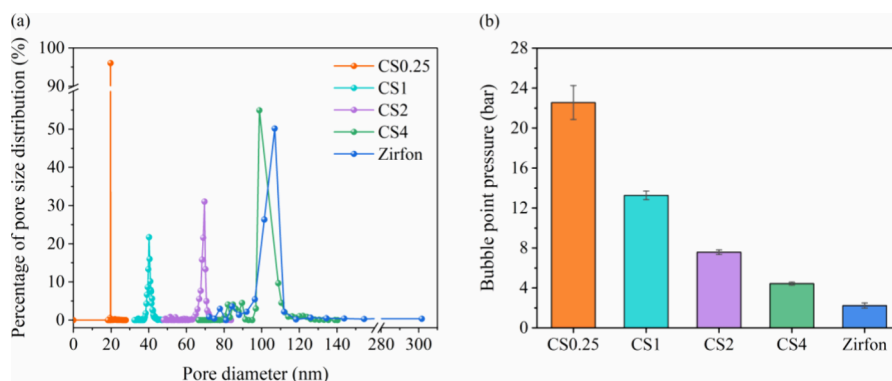
Figure 4. Pore diameter distribution (a) and BPP (b) of the prepared composite separators and Zirfon.

solution and slowed the exchange of the solvent and nonsolvent. Thus, the coarsening process was mitigated, and an interconnected pores/bicontinuous structure was formed via a spinodal decomposition mechanism during the NIPS process.[49]

Figure 3 shows the surface morphologies of the prepared separators. All the prepared separators display relatively dense top surfaces (the surface exposed to air) and submicron porous bottom surfaces (the surface in contact with the glass substrate). Large micron-sized ZrO_2 agglomerates can hardly be observed on both the top and bottom surfaces, indicating that the ZrO_2 nanoparticles are uniformly distributed on both the top and bottom surfaces (Figure S2). For the top surface, the defects in the top surface gradually become severe with the prolonging of pre-evaporation time. For the bottom surface, the longer the time the membrane is exposed to air during the manufacturing process, the larger the pore size the bottom surface has, which is consistent with the cross-sectional morphology results.

3.1.2. Pore Size Analysis and Gas Barrier Property. The pore diameter distributions and gas barrier properties of the separators are depicted in Figure 4. Evidently, the pre-evaporation time has a significant influence on the pore size distributions of the prepared separators. As the pre-evaporation time increases from 15 s to 4 min, the average pore size of the separator increases from 20 to 104 nm (Table 1), and the BPP

Table 1. Pore Diameter of the Composite Separators

sample	CS0.25	CS1	CS2	CS4	Zirfon
maximum pore diameter (nm)	28	47	84	140	302
average pore diameter (nm)	20	41	69	104	108
minimum pore diameter (nm)	18	33	48	67	72
pore size distribution width (nm)	10	14	36	73	230

decreases from 22.6 to 4.4 bar accordingly, which agrees with the SEM morphology results. Compared with the commercial Zirfon, the prepared separators display smaller average pore diameters. To quantitatively compare the narrowness of the pore size distribution for different composite separators, the pore size distribution width was also estimated based on the maximum and minimum pore diameters. Compared with the commercial Zirfon, the prepared composite separators show significantly smaller pore size distribution widths, confirming that the prepared composite separators have a narrower pore size distribution than the commercial Zirfon. As a result, the prepared separators exhibit significantly higher BPPs than the Zirfon membrane (2.2 bar). Additionally, the BPP calculated

for Zirfon is almost the same as that reported by the manufacturer, implying good repeatability and measurement accuracy. The ultrahigh BPPs of the prepared separators indicate that the gas crossover via gas permeability across the separator can be effectively suppressed and the gas barrier requirement (3 bar, corresponding to a maximum pore diameter: ∼200 nm) can be satisfied for industrial applications.[44]

3.1.3. Ion-Transport Property. The area resistance is commonly used as a significant indicator of the ion-transport property of the separators, which depends mainly on its pore structure and wettability.[44] Figure 5 presents the porosity, contact angle, alkaline absorption ratio, and area resistance results of the prepared separators. Low standard deviations are observed for these measurements, indicating a relatively high repeatability and accuracy. The porosities of all the prepared separators exceed 70%, which is much higher than the commercial Zirfon counterpart (56.5%). Since the prepared separators are confirmed to have smaller nanopores (Figure 4), their significantly high porosities can be ascribed to their high interconnectivity of the nanopores (bicontinuous structure). As the pre-evaporation time increases, the porosity of the separator gradually increases due to the growing pore size. The hydrophilicity of the separator can be reflected by the water contact angle. In general, high hydrophilicity is conducive to achieving low area resistance and good electrolysis performance. The contact angle of the top surface of the separator slightly increases with an increasing pre-evaporation time, implying that prolonging the pre-evaporation time adversely affects the hydrophilicity. Considering that the hydrophilicity of the membranes is mainly contributed by the hydrophilic ZrO_2 nanoparticles, and the nominal contents of ZrO_2 are the same for different separators, the deterioration in hydrophilicity with a prolonged pre-evaporation time can be plausibly attributed to the decreased dispersion of ZrO_2 nanoparticles on the membrane surface. It is conceivable that as the pore size increases with an increasing pre-evaporation time, the shedding of ZrO_2 nanoparticles on the membrane surface becomes more severe. Consequently, the dispersion of ZrO_2 on the membrane surface decreases. The alkaline absorption ratio data displays a nonlinear variation with an increasing pre-evaporation time, which is caused by the synthetic effect of the porosity, pore size, and wettability of the separators.[44] Among the prepared separators, CS2 exhibits the lowest area resistance of 0.11 $\Omega \cdot cm^2$ and the highest alkaline absorption ratio of 55.5%, suggesting that CS2 possesses superior electrolyte transport ability.
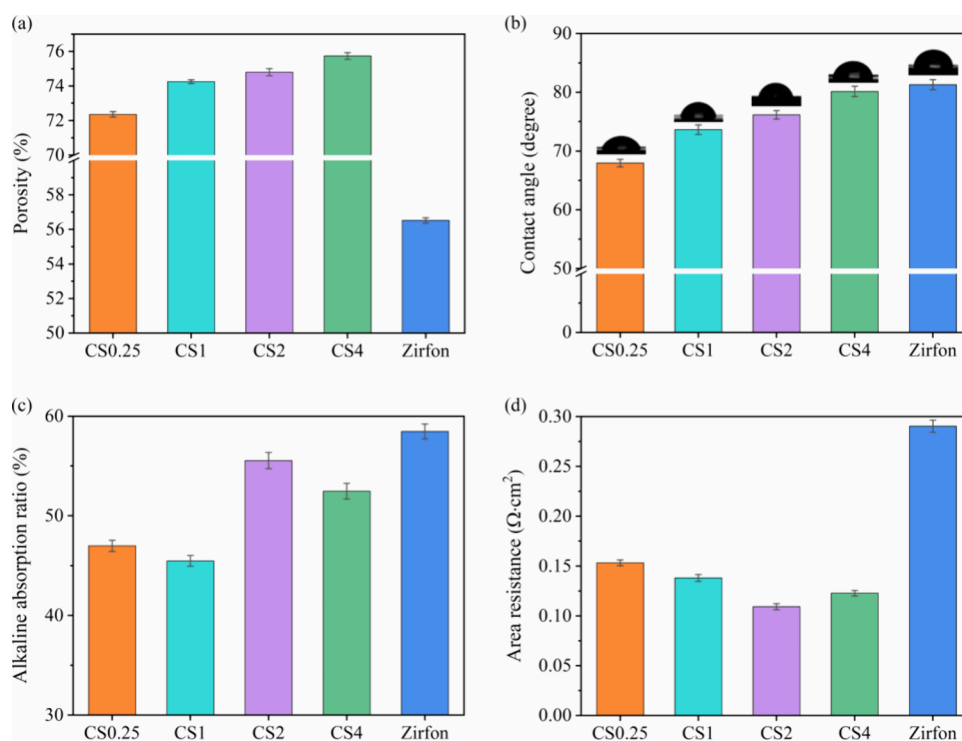
Figure 5. (a) Porosity, (b) contact angle, (c) alkaline absorption ratio, and (d) area resistance of the prepared composite separators and Zirfon.
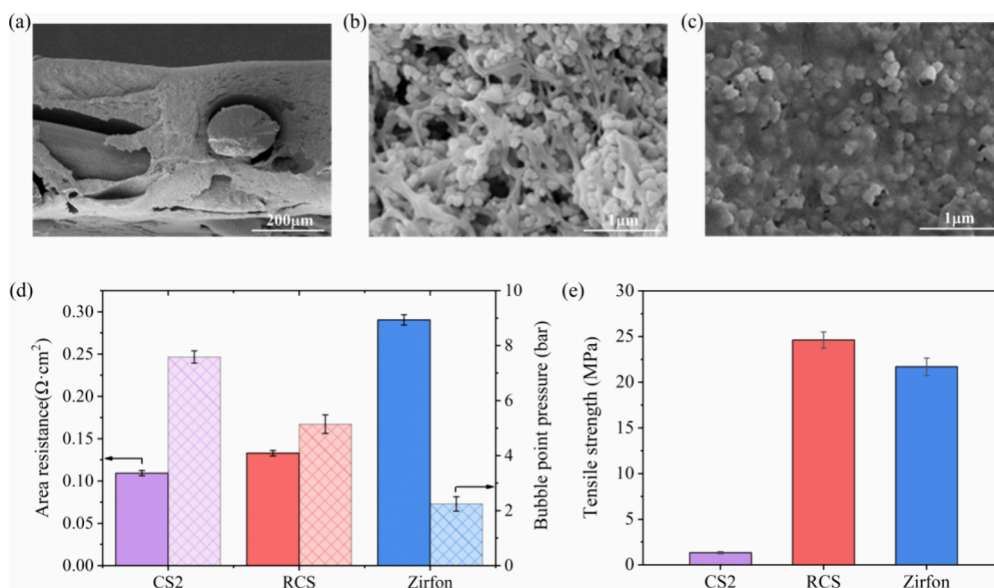

Figure 6. Morphologies and physicochemical properties of the separators: Cross-sectional SEM images of the RCS (a) at 500× magnification and (b) at 100,000× magnification. (c) Top surface SEM image of the RCS at 100,000× magnification. (d) Area resistance and BPP and (e) tensile strength of the prepared composite separators and Zirfon.

These structure and property characterizations reveal that with the extension of the pre-evaporation time, the pore diameter of the composite separator increases. As a result, the porosity increases, whereas the BPP decreases. However, the hydrophilicity deteriorates as the pre-evaporation time increases. As a balance between the porosity and hydrophilicity, the CS2 separator with a pre-evaporation time of 2 min demonstrates superior electrolyte transport ability with a low area resistance of 0.11 $\Omega \cdot cm^2$. Thanks to the relatively narrow pore diameter distribution, the CS2 maintains a high BPP of 7.5 bar. Based on the above analysis, an optimal pre-

evaporation time of 2 min was applied in the preparation of the RCS separator.

3.2. Characterization of the Reinforced Composite Separator. *3.2.1. Morphology and Physicochemical Property.* Pristine composite separators consisting of PSF and ZrO_2 generally display poor mechanical properties of 1−2 MPa (Table S2), which cannot meet the industrial requirements. To further improve the mechanical properties of the optimized CS2 membrane, a PPS-reinforced composite separator, RCS was prepared using similar manufacturing parameters. The prepared RCS has a size of ~30 cm × 30 cm and there are no

Table 2. Summary of the Performance Parameters of Separators

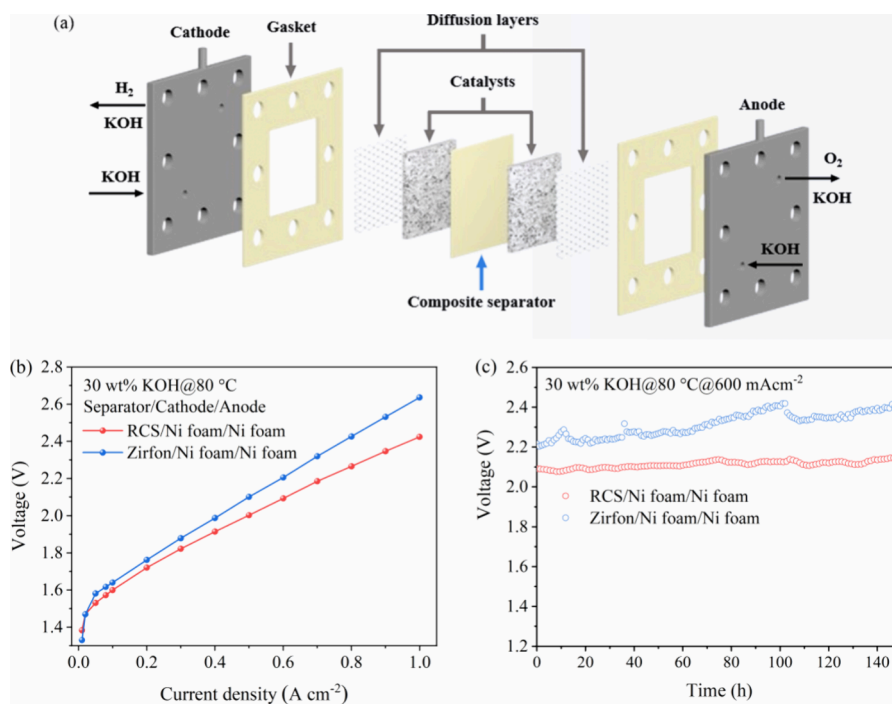| sample	thickness (μm)	average pore diameter (nm)	maximum pore diameter (nm)	porosity (%)	alkaline absorption ratio (%)	contact angle (°)
RCS	447 ± 8	73	124	74.2 ± 0.08	51.4 ± 0.52	72 ± 0.8
Zirfon	504 ± 5	108	302	56.5 ± 0.16	58.5 ± 0.75	81 ± 0.9

Figure 7. Alkaline water electrolysis performance of the composite separators. (a) Schematic illustration of the customized alkaline electrolyzer. (b) Polarization curves of the electrolytic cell using various separators and nickel-based electrodes. (c) Voltage−time plots for the separators at a constant current density of 600 mA cm^{-2} in 30 wt % KOH at 80 °C.

obvious defects on the surface (Figure S3). The crystal structure of the RCS membrane was confirmed by XRD (Figure S4), and diffraction peaks assigned to monoclinic ZrO$_2$ were detected.[51,52] The actual ZrO$_2$ content in the RCS separator was determined to be 77.4% by ICP-OES (Table S3). As shown in Figure 6, the RCS shows a relatively dense top surface and underneath a porous bicontinuous structure in the thickness direction. According to the literature,[49] the membranes with bicontinuous structures are conducive to high porosity and faster permeation due to their highly interconnected pores despite the absence of macrovoids. Consequently, the RCS exhibits a low area resistance of 0.13 $\Omega \cdot$cm^2 and a high BPP of 5.1 bar, which largely outperforms the commercial Zirfon. With the insertion of PPS mesh, the tensile strength of RCS is sharply enhanced to 24.4 MPa, which is slightly higher than the commercial Zirfon counterpart (22.2 MPa). This result demonstrates that the RCS separator can fully meet the mechanical requirements for industrial applications.[53]

The thickness, pore structure parameters, wettability, and alkaline absorption ratio of the RCS are listed in Table 2. The membrane thickness of the RCS was 447 ± 8 μm, indicating a relatively uniform membrane thickness. Similar to the pristine composite separators without a support layer, the RCS shows a much higher porosity (74.2%), narrow pore size distribution with a smaller average pore diameter (73 nm) and a lower contact angle than the commercial Zirfon, which reinforces the superiority of the bicontinuous structure. The RCS exhibits a slightly lower alkaline absorption ratio than Zirfon, which is

mainly attributed to its smaller pore diameter. These results indicate that the low area resistance of RCS is mainly associated with its high porosity and good hydrophilicity and the high BPP is assigned to the narrow pore size distribution with a small pore diameter.

3.2.2. Water Electrolysis Performance and Durability. To assess the practical application potential of the RCS separator in advanced AWE, we investigated the electrolysis performance of electrolytic cells equipped with the prepared separator using nickel foams as cathode and anode (Figure 7a). Zirfon was used as the reference separator. As depicted in Figure 7b, a cell voltage of 2.21 V is reached at 600 mA cm^{-2} for the Zirfon separator, and it is reduced to 2.09 V when the RCS separator is employed. Moreover, for the RCS-equipped cell, the current density reaches 500 mA cm^{-2} at 2.0 V, and this current density is higher than those reported in previous studies.[33,42,44] For instance, Xu et al.[42] proposed a PSF-ZrO$_2$ composite separator with a tight skin layer and an underlying finger-type macropore structure. The electrolytic cell displayed a current density of 300 mA cm^{-2} at 2.0 V when the membrane was applied. Recently, Yuan et al.[44] constructed a series of diethanolamine-functionalized ZrO$_2$-based composite separators with high hydrophilicity, and the optimized membrane presented a current density of 485 mA cm^{-2} at 2.0 V. Based on the aforementioned studies, the superior electrolysis performance of the RCS is inferred to be closely associated with its high porosity and good hydrophilicity. Furthermore, the long-term electrolysis stability of the RCS was evaluated at a current density of 600 mA cm^{-2} for 150 h. The RCS separator exhibits
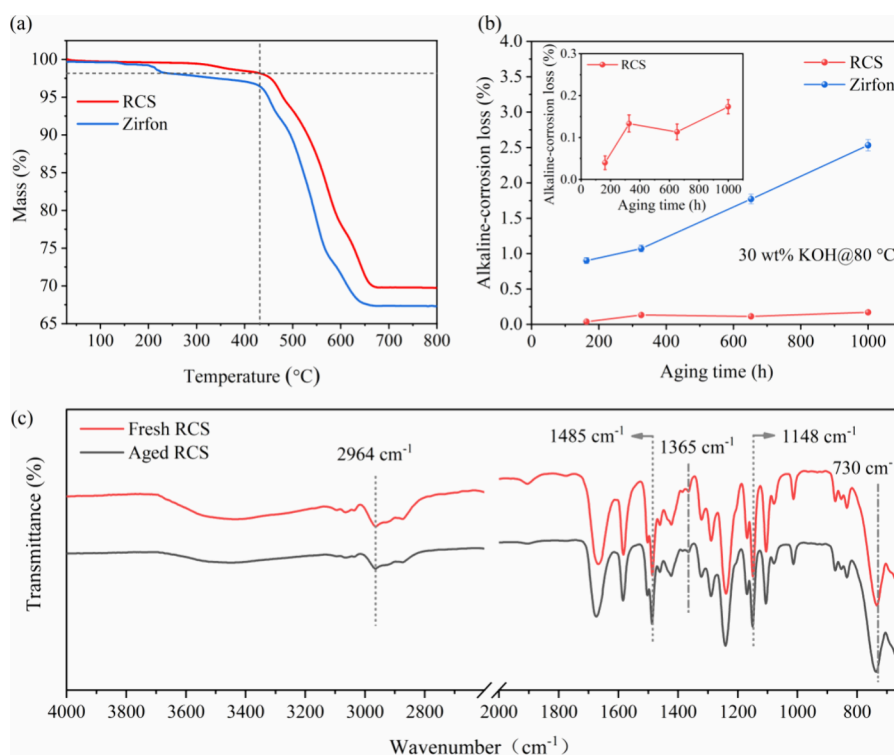
Figure 8. (a) TG profiles of the RCS and Zirfon. (b) Alkaline-corrosion loss of the RCS and Zirfon during the long-term alkaline-aging test, and the inset shows the corresponding enlarged view of RCS. (c) FTIR spectra of the fresh and aged RCS separators. The prepared RCS before and after the test period of 1000 h is denoted as fresh RCS and aged RCS, respectively.

excellent stability during long-term electrolysis (Figure 7c). It started at a relatively low voltage of 2.09 V and ended at a voltage of 2.14 V after 150 h of operation. These results suggest that the RCS can be used as an effective alternative to commercial Zirfon in practical AWE applications.

In an alkaline water electrolyzer, separators are generally exposed to alkaline environments (∼30 wt % KOH) at temperatures of 60−80 °C.[54] Therefore, the separators must maintain good stability in such harsh environments. The thermal and alkaline stabilities of the RCS separator were evaluated in this study (Figure 8). TG (Figure 8a) and DSC (Figure S5) profiles show that the RCS exhibits good thermal stability. The RCS began to decompose around 300 °C and lost 2% mass at 430 °C, ascribed to the removal of residual water.[33,40] The significant mass loss observed over the temperature range of 430−700 °C can be attributed to the polymer backbone degradation of PSF and PPS in the membranes.[55,56] This indicates that the RCS separator can fully meet the operating temperature requirements (60−80 °C) for industrial alkaline electrolyzers.

Long-term alkaline-aging (80 °C, 30 wt % KOH) results (Figure 8b) illustrate that the commercial Zirfon displays an obvious increase in mass loss during the aging process, which is likely caused by the shedding of ZrO_2 nanoparticles from its large porous channels, as verified in Figure S6. By contrast, the RCS separator exhibits an alkaline-corrosion loss of less than 0.2% after 1000 h of operation, indicating excellent alkaline stability. The relatively high standard deviations for RCS are likely due to the extremely low mass loss during the measurement process.

Furthermore, the FTIR spectra of the RCS before and after the long test period (1000 h) were analyzed (Figure 8c). Both the fresh and aged RCS separators exhibit similar FTIR spectral signals related to PSF at 2964 cm^{-1}, 1485 and 1148 cm^{-1}, which are assigned to C−H stretching in the CH_3 group, skeleton vibration of the benzene ring, and symmetric vibration of O=S=O in the sulfone group, respectively. The band at 730 cm^{-1} corresponds to the Zr−O vibration of ZrO_2.[57,58] The band centered at 1365 cm^{-1} is attributed to the vibration of hydroxyl groups on the ZrO_2 surface, which are mainly responsible for the good hydrophilicity of the RCS.[44,59] Additionally, the morphology of the aged RCS separator is similar to that of the fresh RCS separator, and no pore structure damage can be observed in the aged RCS separator (Figure S7). These results consolidate that the RCS maintains excellent stability even after 1000 h of alkaline-aging. A similar phenomenon was found in a previous study.[53] They found that the excellent alkaline stability of the composite separators was mainly dependent on the nature of the membrane materials (PSF and ZrO_2).

Further, we compared the comprehensive performance of the RCS with that of commercial Zirfon (Figure 9). Compared with the Zirfon, our RCS separator exhibits superior performance in terms of the BPP, area resistance, tensile strength, alkaline-corrosion loss, and cell voltage, thereby showing high potential for AWE application.

5. CONCLUSIONS

In this study, novel composite separators with high performance were prepared by using the NIPS method. Bicontinuous structures with an interconnected pore feature formed in the membranes, which endowed the membranes with high porosity, narrow pore size distribution with nanopores, and good hydrophilicity. The average pore size increased whereas the BPP decreased with an increasing pre-evaporation time. A PPS-reinforced composite separator (RCS) was also fabricated.
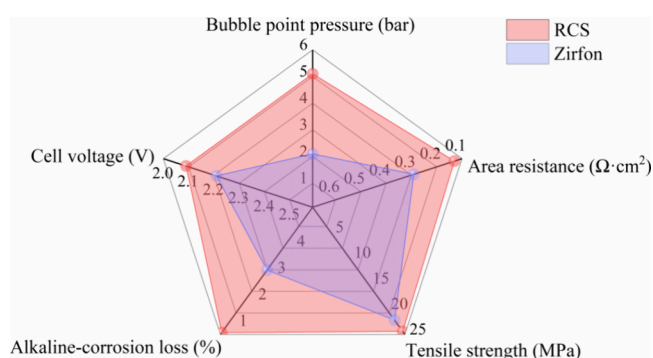
Figure 9. Comprehensive comparison of the properties of RCS and Zirfon, including BPP, area resistance, tensile strength, alkaline-corrosion loss, and cell voltage at 600 mA cm^{-2}.

Thanks to the unique porous bicontinuous structure, the RCS exhibited a high BPP (5.1 bar), low area resistance (0.13 Ω·cm^2), and low cell voltage (2.09 V) at 600 mA cm^{-2}. Moreover, the RCS separator displayed outstanding alkaline stability, and its mass loss was lower than 0.2% after undergoing alkaline aging for 1000 h. Additionally, the RCS maintained excellent long-term electrolysis stability after operating for 150 h at a current density of 600 mA cm^{-2}. The RCS is expected to have significant potential for application in AWE, particularly in high-pressure AWE systems coupled with renewable energy sources.

ASSOCIATED CONTENT

ⓈⒾ Supporting Information

The Supporting Information is available free of charge at https://pubs.acs.org/doi/10.1021/acsomega.4c07167.

> The cross-sectional morphology of the CS-NMP membrane; surface SEM images at 10,000× magnification, and tensile strength of the pristine membranes; photograph, XRD, DSC curve, and ICP analysis of the reinforced membrane; morphology of the Zirfon membrane (PDF)

AUTHOR INFORMATION

Corresponding Authors

Liping Liu − *Huaneng Clean Energy Research Institute, Beijing 102209, China;* ⓞ orcid.org/0009-0007-4223-1017; Email: lp_liu@qny.chng.com.cn

Jinyi Wang − *Huaneng Clean Energy Research Institute, Beijing 102209, China;* Email: jy_wang@qny.chng.com.cn

Authors

Ju Wang − *Huaneng Clean Energy Research Institute, Beijing 102209, China*

Guanjun Yang − *Huaneng Clean Energy Research Institute, Beijing 102209, China*

Shuyuan Wang − *North China Electric Power University, Beijing 102206, China*

Zhibo Ren − *Huaneng Clean Energy Research Institute, Beijing 102209, China*

Weiqi Guo − *Huaneng Clean Energy Research Institute, Beijing 102209, China*

Peng Liu − *Huaneng Clean Energy Research Institute, Beijing 102209, China*

Complete contact information is available at:
https://pubs.acs.org/10.1021/acsomega.4c07167

REFERENCES

(1) Veziroğlu, T. N.; Şahin, S. 21st Century's energy: Hydrogen energy system. *Energy Convers. Manage.* **2008**, 49 (7), 1820−1831.

(2) Blanco, H.; Faaij, A. A review at the role of storage in energy systems with a focus on Power to Gas and long-term storage. *Renew. Sust. Energy Rev.* **2018**, 81, 1049−1086.

(3) Nikolaidis, P.; Poullikkas, A. A comparative overview of hydrogen production processes. *Renew. Sust. Energy Rev.* **2017**, 67, 597−611.

(4) Ma, H.; Zhu, H.; Wang, Z. Highly alkaline stable anion exchange membranes from nonplanar polybenzimidazole with steric hindrance backbone. *J. Polym. Sci., Polym. Chem.* **2019**, 57 (10), 1087−1096.

(5) Li, H.; Hu, X.; Geng, K.; Liu, M.; Hu, B.; Chen, Q.; Jiang, Z.; He, M.; Huang, Y.; Li, N.; Xu, Z.; Zhang, Q. Highly hydrophilic polybenzimidazole/Zirconia composite separator with reduced gas crossover for alkaline water electrolysis. *J. Membr. Sci.* **2023**, 683, No. 121844.

(6) Kumar, S. S.; Himabindu, V. Hydrogen production by PEM water electrolysis-A review. *Mater. Sci. Energy Technol.* **2019**, 2 (3), 442−454.

(7) Tenhumberg, N.; Büker, K. Ecological and economic evaluation of hydrogen production by different water electrolysis technologies. *Chem. Ing. Technol.* **2020**, 92 (10), 1586−1595.

(8) Dawood, F.; Anda, M.; Shafiullah, G. M. Hydrogen production for energy: An overview. *Int. J. Hydrogen Energy* **2020**, 45 (7), 3847−3869.

(9) David, M.; Ocampo-Martínez, C.; Sánchez-Peña, R. Advances in alkaline water electrolyzers: A review. *J. Energy Storage* **2019**, 23, 392−403.

(10) Schmidt, O.; Gambhir, A.; Staffell, I.; Hawkes, A.; Nelson, J.; Few, S. Future cost and performance of water electrolysis: An expert elicitation study. *Int. J. Hydrogen Energy* **2017**, 42 (52), 30470−30492.

(11) Lu, C.; Long, C.; Li, Y.; Li, Z.; Zhu, H. Chemically stable poly(meta-terphenyl piperidinium) with highly conductive side chain for alkaline fuel cell membranes. *J. Membr. Sci.* **2020**, 598, No. 117797.

(12) Daoudi, C.; Bounahmidi, T. Overview of alkaline water electrolysis modeling. *Int. J. Hydrogen Energy* **2024**, 49, 646−667.

(13) Lee, B.; Cho, H.-S.; Kim, H.; Lim, D.; Cho, W.; Kim, C.-H.; Lim, H. Integrative techno-economic and environmental assessment for green H₂ production by alkaline water electrolysis based on experimental data. *J. Environ. Chem. Eng.* **2021**, 9 (6), No. 106349.

(14) Ju, W.; Heinz, M. V. F.; Pusterla, L.; Hofer, M.; Fumey, B.; Castiglioni, R.; Pagani, M.; Battaglia, C.; Vogt, U. F. Lab-scale alkaline water electrolyzer for bridging material fundamentals with realistic operation. *ACS Sustain. Chem. & Eng.* **2018**, 6 (4), 4829−4837.

(15) Zhu, H.; Li, Y.; Chen, N.; Lu, C.; Long, C.; Li, Z.; Liu, Q. Controllable physical-crosslinking poly(arylene 6-azaspiro[5.5] undecanium) for long-lifetime anion exchange membrane applications. *J. Membr. Sci.* **2019**, 590, No. 117307.

(16) Niblett, D.; Delpisheh, M.; Ramakrishnan, S.; Mamlouk, M. Review of next generation hydrogen production from offshore wind using water electrolysis. *J. Power Sources* **2024**, 592, No. 233904.

(17) Kazemi, A.; Manteghi, F.; Tehrani, Z. Metal electrocatalysts for hydrogen production in water splitting. *ACS Omega* **2024**, 9, 7310−7335.

(18) Amireh, S. F.; Heineman, N. N.; Vermeulen, P.; Barros, R. L. G.; Yang, D.; van der Schaaf, J.; de Groot, M. T. Impact of power supply fluctuation and part load operation on the efficiency of alkaline water electrolysis. *J. Power Sources* **2023**, 560, No. 232629.

(19) Alam, A.; Park, C.; Lee, J.; Ju, H. Comparative analysis of performance of alkaline water electrolyzer by using porous separator and ion-solvating polybenzimidazole membrane. *Renew. Energy* 2020, *166*, 222−233.

(20) Baum, Z. J.; Diaz, L. L.; Konovalova, T.; Zhou, Q. A. Materials research directions toward a green hydrogen economy: A review. *ACS Omega* 2022, *7* (37), 32908−32935.

(21) Modica, G.; Giuffre, L.; Montoneri, E.; Pozzi, V.; Tempesti, E. Electrolytic separators from asbestos cardboard: A flexible technique to obtain reinforced diaphragms or ion-selective membranes. *Int. J. Hydrogen Energy* 1983, *8* (6), 419−435.

(22) Rodríguez, J.; Palmas, S.; Sánchez-Molina, M.; Amores, E.; Mais, L.; Campana, R. Simple and precise approach for determination of ohmic contribution of diaphragms in alkaline water electrolysis. *Membranes* 2019, *9* (10), 129.

(23) Wan, L.; Xu, Z.; Wang, B. Green preparation of highly alkali-resistant PTFE composite membranes for advanced alkaline water electrolysis. *Chem. Eng. J.* 2021, *426*, No. 131340.

(24) Wang, Y.; Huo, X.; Peng, M.; Zhang, M.; Liu, X.; Zhang, J.; Li, W. Superhydrophilic polyphenylene sulfide membrane with enhanced ion transfer for alkaline water electrolysis. *Int. J. Hydrogen Energy* 2024, *65*, 872−880.

(25) Vermeoren, P.; Adriansens, W.; Moreels, J. P.; Leysen, R. Evaluation of the Zirfon separator for use in alkaline water electrolysis and Ni-H$_2$ batteries. *Int. J. Hydrogen Energy* 1998, *23*, 321−324.

(26) Vermeiren, P. H.; Leysen, R.; Beckers, H.; Moreels, J. P.; Claes, A. The influence of manufacturing parameters on the properties of macroporous Zirfon® separators. *J. Porous Mater.* 2008, *15* (3), 259−264.

(27) Vermeiren, P.; Adriansens, W.; Leysen, R. Zirfon: A new separator for Ni-H$_2$ Batteries and alkaline fuel cells. *Int. J. Hydrogen Energy* 1996, *21*, 679−684.

(28) Kim, S.; Han, J. H.; Yuk, J.; Kim, S.; Song, Y.; So, S.; Lee, K. T.; Kim, T.-H. Highly selective porous separator with thin skin layer for alkaline water electrolysis. *J. Power Sources* 2022, *524*, No. 231059.

(29) Liao, Y.; Deng, G.; Ding, L.; Wang, H. A thin and flexible composite membrane with low area resistance and high bubble point pressure for advanced alkaline water electrolysis. *J. Membr. Sci.* 2024, *689*, No. 122182.

(30) Altaf, C. T.; Colak, T. O.; Karagoz, E.; Kurt, M.; Sankir, N. D.; Sankir, M. A review of the recent advances in composite membranes for hydrogen generation technologies. *ACS Omega* 2024, *9*, 23138−23154.

(31) Liao, Y.; Deng, G.; Wu, H.; Ding, L.; Wang, H. A porous skeleton-supported organic/inorganic composite membrane for high-efficiency alkaline water electrolysis. *Adv. Funct. Mater.* 2023, *34* (3), No. 2309871.

(32) Lee, H. I.; Mehdi, M.; Kim, S. K.; Cho, H. S.; Kim, M. J.; Cho, W. C.; Rhee, Y. W.; Kim, C. H. Advanced Zirfon-type porous separator for a high-rate alkaline electrolyser operating in a dynamic mode. *J. Membr. Sci.* 2020, *616*, No. 118541.

(33) Lee, J. W.; Lee, J. H.; Lee, C. S.; Cho, H. S.; Kim, M. J.; Kim, S. K.; Joo, J. H.; Cho, W. C.; Kim, C. H. Cellulose nanocrystals−blended zirconia/polysulfone composite separator for alkaline electrolyzer at low electrolyte contents. *Chem. Eng. J.* 2022, *428*, No. 131149.

(34) Ali, M. F.; Lee, H. I.; Bernacker, C. I.; Weissgarber, T.; Lee, S.; Kim, S. K.; Cho, W. C. Zirconia toughened alumina-based separator membrane for advanced alkaline water electrolyzer. *Polymers* 2022, *14* (6), 1173.

(35) Shiva Kumar, S.; Ramakrishna, S. U. B.; Krishna, S. V.; Srilatha, K.; Devi, B. R.; Himabindu, V. Synthesis of titanium (IV) oxide composite membrane for hydrogen production through alkaline water electrolysis. *S. Afr. J. Chem. Eng.* 2018, *25*, 54−61.

(36) Kuleshov, N. V.; Kuleshov, V. N.; Dovbysh, S. A.; Udris, E. Y.; Grigor'ev, S. A.; Slavnov, Y. A.; Korneeva, L. A. Polymeric composite diaphragms for water electrolysis with alkaline electrolyte. *Russ. J. Appl. Chem.* 2016, *89* (4), 618−621.

(37) Burnat, D.; Schlupp, M.; Wichser, A.; Lothenbach, B.; Gorbar, M.; Züttel, A.; Vogt, U. F. Composite membranes for alkaline

electrolysis based on polysulfone and mineral fillers. *J. Power Sources* 2015, *291*, 163−172.

(38) Ali, M. F.; Cho, H.-S.; Bernäcker, C. I.; Albers, J.; Young-Woo, C.; Kim, M.; Lee, J. H.; Lee, C.; Lee, S.; Cho, W.-C. A study on the effect of TiO$_2$ nanoparticle size on the performance of composite separators in alkaline water electrolysis. *J. Membr. Sci.* 2023, *678*, No. 121671.

(39) Lee, J. W.; Lee, C.; Lee, J. H.; Kim, S. K.; Cho, H. S.; Kim, M.; Cho, W. C.; Joo, J. H.; Kim, C. H. Cerium oxide-polysulfone composite separator for an advanced alkaline electrolyzer. *Polymers* 2020, *12* (12), 2821.

(40) In Lee, H.; Dung, D. T.; Kim, J.; Pak, J. H.; Kim, S. k.; Cho, H. S.; Cho, W. C.; Kim, C. H. The synthesis of a Zirfon-type porous separator with reduced gas crossover for alkaline electrolyzer. *Int. J. Energy Res.* 2020, *44* (3), 1875−1885.

(41) Otero, J.; Sese, J.; Michaus, I.; Santa Maria, M.; Guelbenzu, E.; Irusta, S.; Carrilero, I.; Arruebo, M. Sulphonated polyether ether ketone diaphragms used in commercial scale alkaline water electrolysis. *J. Power Sources* 2014, *247*, 967−974.

(42) Xu, L.; Li, W.; You, Y.; Zhang, C.; Zhao, Y. Polysulfone and zirconia composite separators for alkaline water electrolysis. *Front. Chem. Sci. Eng.* 2013, *7* (2), 154−161.

(43) Xu, L.; Yu, Y.; Li, W.; You, Y.; Xu, L.; Zhang, C. The influence of manufacturing parameters and adding support layer on the properties of Zirfon® separators. *Front. Chem. Sci. Eng.* 2014, *8* (3), 295−305.

(44) Yuan, X.; Yan, T.; Liu, Z.; Kang, P. Highly efficient alkaline water electrolysis using alkanolamine-functionalized zirconia-blended separators. *ACS Sustain. Chem. & Eng.* 2023, *11* (10), 4269−4278.

(45) Xu, M.-H.; Xie, R.; Ju, X.-J.; Wang, W.; Liu, Z.; Chu, L.-Y. Antifouling membranes with bi-continuous porous structures and high fluxes prepared by vapor-induced phase separation. *J. Membr. Sci.* 2020, *611*, No. 118256.

(46) Wang, H. H.; Jung, J. T.; Kim, J. F.; Kim, S.; Drioli, E.; Lee, Y. M. A novel green solvent alternative for polymeric membrane preparation via nonsolvent-induced phase separation (NIPS). *J. Membr. Sci.* 2019, *574*, 44−54.

(47) Hung, W.-L.; Wang, D.-M.; Lai, J.-Y.; Chou, S.-C. On the initiation of macrovoids in polymeric membranes-effect of polymer chain entanglement. *J. Membr. Sci.* 2016, *505*, 70−81.

(48) Tsai, J. T.; Su, Y. S.; Wang, D. M.; Kuo, J. L.; Lai, J. Y.; Deratani, A. Retainment of pore connectivity in membranes prepared with vapor-induced phase separation. *J. Membr. Sci.* 2010, *362* (1−2), 360−373.

(49) Maggay, I. V.; Yu, M. L.; Wang, D. M.; Chiang, C. H.; Chang, Y.; Venault, A. Strategy to prepare skin-free and macrovoid-free polysulfone membranes via the NIPS process. *J. Membr. Sci.* 2022, *655*, No. 120597.

(50) Chavda, V.; Patel, H. D.; Patel, A. K.; Hirpara, D.; Acharya, N. K.; Kumar, S. Deep eutectic solvent engineered GO / ZrO$_2$ nanofiller for mixed matrix membranes: An efficient hydrogen gas separation. *J. Appl. Polym. Sci.* 2024, *141*, No. e55938.

(51) Wang, X.; Liu, L.; Wang, X.; Bai, X.; Qin, J.; Li, X.; Wang, B. Joule heat induced ultrafine ZrO$_2$/C composites for enhanced microwave absorption. *Surf. Interfaces* 2024, *51*, No. 104818.

(52) Wu, X.; Tan, M.; Xu, B.; Zhao, S.; Ma, Q.; He, Y.; Zeng, C.; Yang, G.; Tsubaki, N.; Tan, Y. Tuning the crystallite size of monoclinic ZrO$_2$ to reveal critical roles of surface defects on m-ZrO$_2$ catalyst for direct synthesis of isobutene from syngas. *Chin. J. Chem. Eng.* 2021, *35*, 211−219.

(53) Liu, L.; Wang, J.; Ren, Z.; Wang, F.; Wang, T.; Guo, H. Ultrathin reinforced composite separator for alkaline water electrolysis: Comprehensive performance evaluation. *Int. J. Hydrogen Energy* 2023, *48*, 23885−23893.

(54) Wan, L.; Xu, Z. A.; Wang, P.; Xu, Q.; Wang, B. Progress of alkaline-resistant ion membranes for hydrogen production by water electrolysis. *Chem. Ind. Eng. Prog.* 2022, *41* (3), 1556−1568.

(55) Li, Z.; Wu, M.; Wang, X.; Yang, F.; Jia, Y.; Zhu, Z.; Xiong, S.; Wang, L. Thermal decomposition and charring behavior of

polyphenylene sulfide/para-amrid fiber composite paper with excellent fireproof property. *React. Funct. Polym.* **2024**, *194*, No. 105761.

(56) Kocakulak, T.; Taşkın, G.; Tabanlıgil Calam, T.; Solmaz, H.; Calam, A.; Arslan, T. A.; Şahin, F. A new nanocomposite membrane based on sulfonated polysulfone boron nitride for proton exchange membrane fuel cells: Its fabrication and characterization. *Fuel* **2024**, *374*, No. 132476.

(57) Jithin, P. V.; Dhamodaran, A.; Prajisha, K. P.; Suman, S.; Sankaran, K. J.; Ramesh, A.; K, S.; Kurian, J. Structural and optical properties of Ce-stabilized tetragonal phase and intense blue emission of monoclinic phase in ZrO_2 nanoparticles. *J. Lumin.* **2025**, *277*, No. 120933.

(58) Fang, D.; Luo, Z.; Liu, S.; Zeng, T.; Liu, L.; Xu, J.; Bai, Z.; Xu, W. Photoluminescence properties and photocatalytic activities of zirconia nanotube arrays fabricated by anodization. *Opt. Mater.* **2013**, *35* (7), 1461−1466.

(59) Mohsen, Q.; Al-Gethami, W. S.; Zaki, Z.; Alotaibi, S. H.; Ibrahim, M. M.; Ezzat, M.; Amin, M. A.; Kamel, M. M.; Mostafa, N. Y. Effect of pH on hydrothermal synthesis of ZrO_2 nanoparticles and their electrocatalytic activity for hydrogen production. *Inter. J. Electrochem. Sc.* **2022**, *17* (7), 22073.